Automated markerless full field hard x-ray microscopic tomography at sub-50nm 3-dimension spatial resolution

Jun Wang, Yu-chen Karen Chen, Qingxi Yuan, Andrei Tkachuk, Can Erdonmez et al.

Related Articles

In situ imaging of orthoclase–aqueous solution interfaces with x-ray reflection interface microscopy
J. Appl. Phys. 110, 102211 (2011)

Quantitative study of interior nanostructure in hollow zinc oxide particles on the basis of nondestructive x-ray nanotomography
Appl. Phys. Lett. 95, 053108 (2009)

Imaging the antiparallel magnetic alignment of adjacent Fe and MnAs thin films
Appl. Phys. Lett. 93, 122508 (2008)

Defect structures in B12As2 epitaxial layers grown on (0001) 6H-SiC
J. Appl. Phys. 103, 123508 (2008)

Synchrotron x-ray microscopy studies on electromigration of a two-phase material
J. Appl. Phys. 102, 053507 (2007)

Additional information on Appl. Phys. Lett.

Journal Homepage: http://apl.aip.org/

Journal Information: http://apl.aip.org/about/about_the_journal

Top downloads: http://apl.aip.org/features/most_downloaded

Information for Authors: http://apl.aip.org/authors

Automated markerless full field hard x-ray microscopic tomography at sub-50 nm 3-dimension spatial resolution

Jun Wang,[1,a] Yu-chen Karen Chen,[1] Qingxi Yuan,[1] Andrei Tkachuk,[2] Can Erdonmez,[3] Benjamin Hornberger,[2] and Michael Feser[2]

[1]*Photon Science Directorate, Brookhaven National Laboratory, Upton, New York 11973, USA*
[2]*Xradia Inc., 4385 Hopyard Rd., Pleasanton, California 94588, USA*
[3]*Sustainable Energy Technologies Department, Brookhaven National Laboratory, Upton, New York 11973, USA*

A full field transmission x-ray microscope (TXM) has been developed and commissioned at the National Synchrotron Light Source at Brookhaven National Laboratory. The capabilities we developed in auto-tomography, local tomography, and spectroscopic imaging that overcome many of the limitations and difficulties in existing transmission x-ray microscopes are described and experimentally demonstrated. Sub-50 nm resolution in 3-dimension (3D) with markerless automated tomography has been achieved. These capabilities open up scientific opportunities in many research fields. © 2012 American Institute of Physics. [http://dx.doi.org/10.1063/1.3701579]

Structural information at nanometer scales plays an increasingly important role in the research and development across many disciplines of science and engineering today, including energy storage, nanoporous materials functions, microelectronics, as well as heterogeneous systems in environmental and biological sciences. In all these fields, a critical research need is the ability to quantitatively image complex structural evolution nondestructively in 3D at nanometer scale and under *in-situ* conditions so that such structural information can be easily correlated to the materials or device functions. In recent years, full-field hard x-ray transmission microscopy has rapidly emerged as a powerful tool to satisfy this research need.

Despite many successful researches[1–6] using hard x-ray transmission x-ray microscope (TXM), existing nano-tomography TXM systems have several difficulties in 3D tomography reconstructions that may limit their wide-spread applications. The difficulties arise mainly from the need to manually align the projection images at different viewing angles by the use of sharp internal features in the specimen or by the introduction of fiducial external markers. This generally limits the type of samples that one can study, especially when observations of local regions of interest (so-called local tomography) are desired. This also often limits the number of images collected because of the need for manual alignment of 2D projections, which considerably affects 3D structure resolution. Another difficulty for spectroscopic imaging is that the images collected at several x-ray energies around one or more atomic absorption edges have to be resampled to match their pixel sizes to each other, making it difficult to obtain high-fidelity structural information such as object shape and curvature without sacrificing spatial resolution.

In this paper, we present the experimental test results of a TXM that has been designed and implemented to overcome the limitations discussed above. These results demonstrate many advanced capabilities such as automated and local tomography at sub-50 nm resolution in 3D and constant-magnification spectral microscopy.

Automated markerless nano-tomography using TXM is a much-desired imaging technique for many applications. Due to the difficulties in keeping the rotation center stable in nano-tomographic imaging, one usually has to mount a fiducial marker on a sample as a reference to align each 2D projection to reconstruct 3D structure, typically in the form of gold spheres. However, there are a few restrictions for adding the reference. First, it is challenging to mount a single marker on a micron-scale sample. Second, it is not applicable for interior tomography which gives 3D structure of interesting regions internal to the sample. Third, the marker might introduce artifacts such as streaking to the reconstructed image due to residual alignment errors or non-linear effects of the high-density gold material. Auto-alignment based on software tracking of fiducials is being used extensively to achieve automated tomography in soft x-ray microscopy and electron microscopy.[7] However, this automated alignment by computer algorithms requires features in the sample with strong contrast or a fiducial marker. In order to accomplish markerless automated tomography, a key requirement is the precision alignment and stability of the rotation axis during tomographic data collection. At present, the best achievement of the precision of the rotation stage from commercial TXM is about one micron wobble at the sample position. It is critical to develop a system to correct the wobble generated during rotation to lead to an automated 3D tomography. Air-bearing rotation stages have been used to reduce the rotation wobble to obtain sub-micron 3D spatial resolution.[8] In contrast, the TXM, operated on X8C beamline at National Synchrotron Light Source (NSLS), employs a passive rotational run-out correction system[9] which is based on an active feedback run-out correction system described earlier.[10] This system consists of a precision cylinder mounted on a low run-out ball bearing rotation stage and three integrated capacitive sensors as shown in Figure 1(a) to measure the residual run-out of the rotation axis as a function of rotation

---

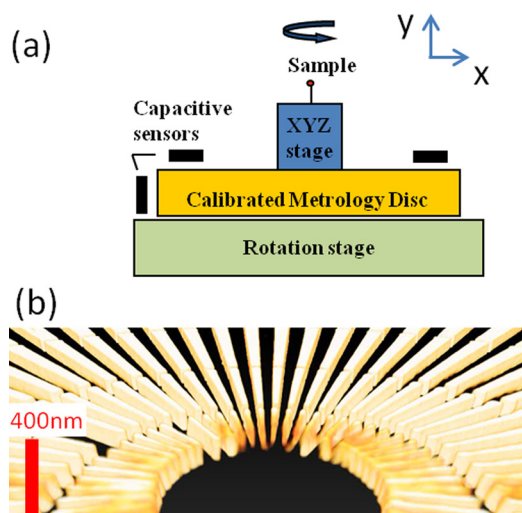[a]Author to whom correspondence should be addressed. Electronic mail: junwang@bnl.gov.

FIG. 1. (a) A schematic showing the run-out correction system which consists of a precision metrology cylinder mounted on a low run-out ball bearing rotation stage and three integrated capacitive sensors to measure the residual run-out of the rotation axis as a function of rotation angle. (b) A zoom-in rendering of a 3D reconstruction of a standard Siemens star pattern with 30 nm finest feature size using automated tomography.

angle. These measured sensor readings are calibrated through multiple sets of tomography data from a standard gold ball with a known $3 \mu m$ diameter. Then, a program[9] reads the calibrated measurements with an algorithm to obtain the run-out corrections $\Delta x(\theta)$ and $\Delta y(\theta)$ at each rotation angle as a function of the measured displacements of the capacitive sensors. When taking a tomography data for a sample, these run-out corrections are automatically applied to produce a transparent mode of usage that emulates a perfect system without any rotational run-out. Without any need for user interaction, each collected 2D projection is automatically aligned for 3D reconstruction to fulfill automated 3D tomography.

We demonstrate the automated nano-tomography capability by two examples. Figure 1(b) shows a zoomed-in rendering of a 3D reconstruction of a standard Siemens star pattern (Xradia X30-30-2) with 30 nm finest feature size acquired with the automated tomography. The Siemens star pattern is made of gold with thickness around 180 nm on a silicon nitride membrane. Because the Si support frame of the silicon nitride window blocks the beam at higher angles, the maximum angle range is limited to $+/-60°$. Throughout this range, we collected 961 images with $0.125°$ step size by taking advantage of the automated tomography. The inner most spokes with 30 nm feature size are clearly separated in

Figure 1(b). It is in agreement with theoretical resolution limit set by the angular step size in tomographic data collection. Due to the restricted angular range, limited angle artifacts are still visible in the reconstructed 3D volume (not shown in Figure 1(b)). Further quantitative study of 3D spatial resolution with a proper sample holding frame to minimize the artifacts is in progress.

The automated 3D tomography was applied to a sintered $LiCoO_2$ electrode of Li-ion battery with feature size less than 100 nm. These porous ceramic electrodes are monolithic, free of the binders, and conductive additives present in conventional Li-ion batteries.[11] Since their power performance is uniquely dictated by the connectivity of pores and particles, it is critical to understand such electrode structures in 3D at a nanometer scale.

The $LiCoO_2$ electrode was prepared by high-speed milling of a commercially available $LiCoO_2$ powder for size reduction, uniaxially pressing the powder into a pellet and sintering the pellet under air at high temperature. The sample for the TXM experiment was milled out from the pellet by focused ion beam (FIB) to a cylindrical shape with a $30 \mu m$ diameter at the Center for Functional Nanomaterials at Brookhaven National Laboratory (BNL). It was mounted on a tungsten pin for the TXM experiment using a standard lift-out procedure in the FIB. Figure 2(a) is a 2D projection image of the $LiCoO_2$ with $40 \mu m$ field of view (FOV) at 8 keV. Tomographic data were collected on a $20 \mu m$ region of the sample shown in Figure 2(a) by the red dashed line. A total of 1441 images were collected over an angular range of $180°$. Without mounting any marker on the sample to align each 2D projection, Figure 2(b) shows the 3D reconstruction structure (cut-view) by applying the automated run-out correction on each image. In order to better show the result by the automated tomography, a part of a reconstructed slice marked by the yellow line in Figure 2(a) is shown in Figure 2(c). Fine features associated with $LiCoO_2$ particles and pores are clearly visible in the cross section from the automated 3D reconstruction with a visible small feature size around 50 nm.

This unique capability of automated markerless tomography allows maximizing the number of images to be collected for tomography to achieve the best resolution for the 3D structure, which is significantly advantageous over a TXM system without such run-out correction, where a 3D structure resolution is considerably affected by limited number of images collected for manual alignment.

With the feature having motorized and encoded sample translation stages above the sample rotation stage, any part of a sample can be easily brought to the center of the rotation
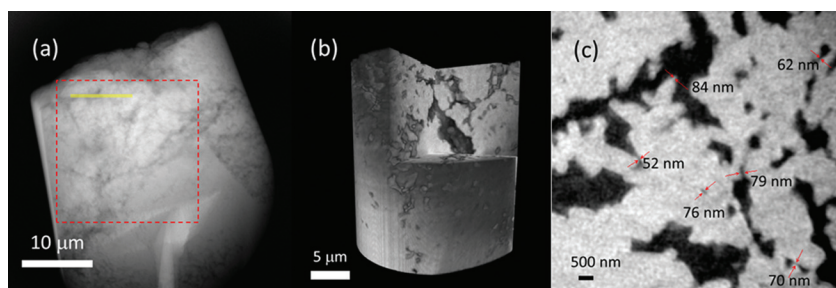

FIG. 2. (a) A 2D projection image of the $LiCoO_2$ electrode with $40 \mu m$ field of view taken at 8 keV. (b) A rendering of the 3D structure of a local region ($20 \mu m$) marked by the red dashed line in (a). (c) A part of a reconstructed slice marked by the yellow line in (a) showing a visible small feature size around 50 nm.
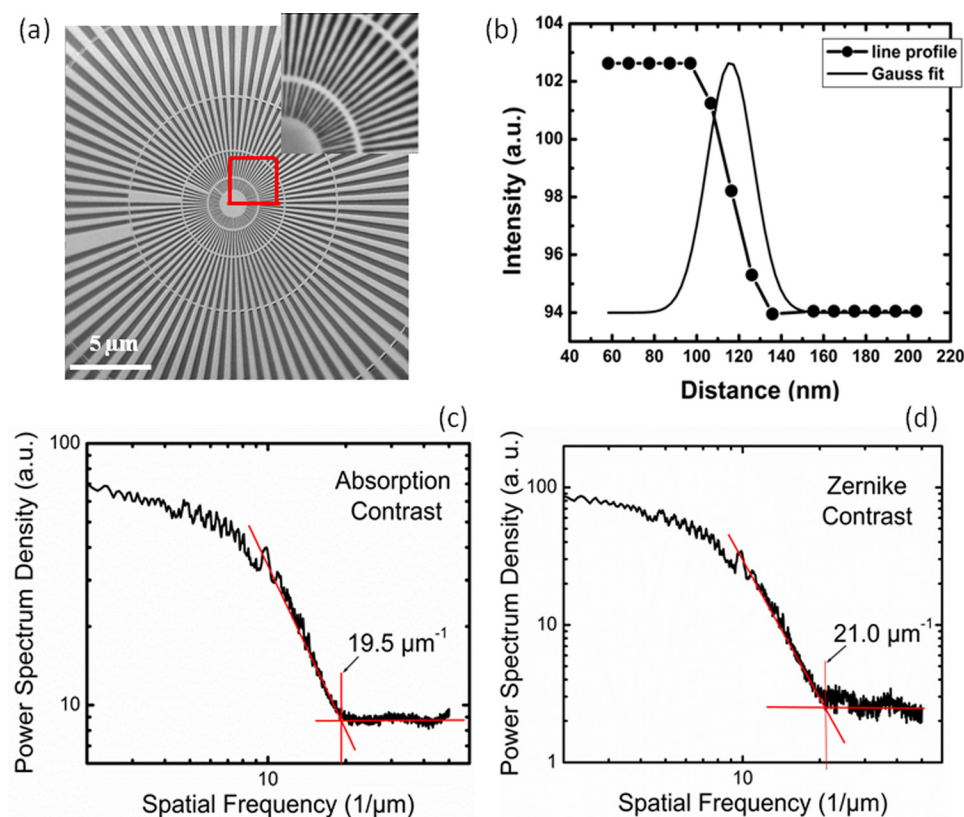
FIG. 3. (a) Siemens Au star pattern with 30 nm finest feature size by absorption contrast with a insert of an enlarged a quarter of center. (b) Knife-edge intensity profile from the sharp feature of the star pattern and Gaussian fit of the differentiated edge response. Power spectrum density analysis on the star patterns by absorption contrast (c) and Zernike phase contrast (d).

axis for tomographic imaging. Combined with the automated markerless tomography capability, this improvement practically enables applications of local nano-tomography. A region of interest on the sample can be identified after reviewing 2D mosaic images at both zero and 90° and translated to the center of the rotation axis to collect tomographic data. The sample can be any shape and bigger than the FOV as long as the overall sample has reasonable transmission at a given x-ray energy. Such local nano-tomography capability opens up an opportunity to practically apply the TXM to bigger samples. Figure 2 illustrates the local tomography capability on the $LiCoO_2$ electrode sample in addition to the automated markerless tomography. Figure 2(b) shows the 3D structure of a local region (20 μm) marked by the red dashed line from a big sample shown in Figure 2(a) without further sample modification.

Spectroscopic imaging enables elemental and chemical information to be obtained.[12] Differential mapping by changing x-ray energy below and above one element absorption edge enhances the contrast of the element and provides quantitative 3D elemental distribution of the element.[1] Since the focal length of a Fresnel zone plate (FZP) f is proportional to the x-ray energy, the image distance $(M + 1)f$, where M is the magnification factor, needs to be adjustable at different energies to keep the same magnification on each image collected at various values of energy. Especially, when a sample has a few elements with absorption edges covering a wide energy range, the distance change is significant to keep the same magnification. In order to fully facilitate full field spectroscopic imaging without sacrificing spatial resolution, the detector of the TXM was designed on a long travel motor-

ized stage to maintain constant imaging magnification by automatically adjusting its position relative to the sample as a function of x-ray energy. This TXM is the only one to accomplish such a requirement to provide the constant magnification. Spectroscopic imaging using this capability is underway and will be published elsewhere.

The 2D spatial resolution of the TXM was investigated with results shown in Figure 3. The objective lens for the testing is a double-stacked[13] FZP with outmost zone width of 30 nm, 100 μm diameter, and total 800 nm thick Au on a silicon nitride membrane. Images of a standard star pattern with 30 nm finest feature size were taken at 8 keV by absorption (Figure 3(a)) and Zernike phase contrast (not shown), respectively. It is clear to distinguish the 30 nm finest feature in the center from both of the images. Quantified evaluation of the spatial resolution was studied by the knife-edge intensity profile with edge response 25%-75%,[14–16] the full width at half-maximum (FWHM)[17,18] of the differentiated curve from an edge, and the power spectrum analysis (PSA).[19–21] With an average of several measurements of sharp features of the star pattern in absorption contrast, the 25%–75% response of the knife-edge intensity profile shown in Figure 3(b) gave 14.2 nm ± 1.5 nm linewidth. Converting it to regular Rayleigh's resolution, it is 24.1 nm ± 2.6 nm by applying a factor of 1.7.[14,15,17] The value of the FWHM of the differentiated edge response in Figure 3(b) is 25.8 nm ± 1.2 nm, which is also viewed as the resolving power. The PSA was performed on the entire star pattern and integrated azimuthally over 2π to evaluate the spatial resolution, as shown in Figure 3(c) for absorption contrast and Fig. 3(d) for Zernike contrast. The cutoff frequency is about 19.5 (1/μm) and 21.0

$(1/\mu m)$, which lead to the spatial resolution of absorption at 25.6 nm and Zernike phase at 23.8 nm. All these results are consistent with each other.

In summary, a state-of-art TXM with unique capabilities has been developed and commissioned at NSLS. The capabilities include markerless auto-tomography, local tomography, and spectroscopic imaging to fully explore advanced imaging techniques. 2D spatial resolution down to 25 nm at hard x-ray for both absorption and Zernike phase contrast has been achieved. The capabilities have led to hard x-ray tomography by TXM with sub-50 nm spatial resolution in 3D. Initial experimental results illustrate great potential for nanometer scale x-ray 3D tomography and will undoubtedly open up new scientific research opportunities in materials research as well as in biology and environmental sciences.

[1]K. N. Grew, Y. S. Chu, J. Yi, A. A. Peracchio, J. R. Izzo, Y. Hwu, F. De Carlo, and W. K. S. Chiu, J. Electrochem. Soc. **157**(6), B783–B792 (2010).

[2]P. C. Hsu, Y. S. Chu, J. Yi, C. L. Wang, S. R. Wu, Y. Hwu, and G. Margaritonodo, Appl. Phys. Lett. **97**, 033101 (2010).

[3]J. C. Andrews, E. Almeida, M. C. H. van der Meulen, J. S. Alwood, C. Lee, Y. Liu, J. Chen, F. Meirer, M. Feser, J. Gelb, J. Rudati, A. Tkachuk, W. Yun, and P. Pianetta, Microsc. Microanal. **16**, 327–336 (2010).

[4]J. Chen, Y. Yang, X. Zhang, J. C. Andrews, P. Pianetta, Y. Guan, G. Liu, Y. Xiong, Z. Wu, and Y. Tian, Anal. Bioanal. Chem. **397**, 2117–2121 (2010).

[5]P. R. Shearing, J. Gelb, J. Yi, W. K. Lee, M. Drakopolous, and N. P. Brandon, Electrochem. Commun. **12**, 1021 (2010).

[6]Y. C. K. Chen, Y. S. Chu, J. M. Yi, I. McNulty, Q. Shen, P. W. Voorhees, and D. C. Dunand, Appl. Phys. Lett. **96**, 043122 (2010).

[7]D. Y. Parkinson, G. McDermott, L. D. Etkin, M. A. Le Gros, and C. A. Larabell, J. Struct. Biol. **162**, 380–386 (2008); M. A. Le Gros, G. McDermott, and C. A. Larabell, Curr. Opin. Struct. Biol. **15**, 593–600 (2005).

[8]M. Stampanoni, A. Groso, A. Isenegger, G. Mikuljan, Q. Chen, A. Bertrand, S. Henein, R. Betemps, U. Frommherz, P. Bohler, D. Meister, M. Lange, and R. Abela, Proc. SPIE **6318**, 6318M (2006); G. Martínez-Criado, R. Tucoulou, P. Cloetens, P. Bleuet, S. Bohic, J. Cauzid, I. Kieffer, E. Kosior, S. Labouré, S. Petitgirard, A. Rack, J. A. Sans, J. Segura-Ruiz, H. Suhonen, J. Susini, and J. Villanova, J. Synchrotron. Radiat. **19**, 10–18 (2012).

[9]Xradia Inc., patent pending.

[10]Xradia Inc., U.S. Patent No. 7,535,193 B2. (U.S. Patent and Trademark Office, Washington, DC, May 19, 2009).

[11]W. Lai, C. K. Erdonmez, T. F. Marinis, C. K. Bjune, N. J. Dudney, F. Xu, R. Wartena, and Y.-M. Chiang, Adv. Mater. **20**, E139 (2010).

[12]F. Meirer, J. Cabana, Y. Liu, A. Mehta, J. C. Andrews, and P. Pianetta, J. Synchrotron Radiat. **18**, 773–781- (2011).

[13]Y. Feng, M. Feser, A. Lyon, S. rishton, X. Zeng, S. Chen, S. Sassolini, and W. Yun, J. Vac. Sci. Technol. B, **25**, 2004 (2007).

[14]Y. Horikawa, J. Opt. Soc. Am. A **11**, 1985 (1994).

[15]Y. S. Chu, J. M. Yi, F. De Carlo, Q. Shen, W.-K. Lee, H. J. Wu, C. L. Wang, J. Y. Wang, C. J. Liu, C. H. Wang, S. R. Wu, C. C. Chien, Y. Hwu, A. Tkachuk, W. Yun, M. Feser, K. S. Liang, C. S. Yang, J. H. Je, and G. Margaritondo, Appl. Phys. Lett. **92**, 103119 (2008).

[16]G.-C. Yin, M.-T. Tang, Y.-F. Song, F.-R. Chen, K. S. Liang, F. W. Duewer, W. Yun, C.-H. Ko, and H.-P. D. Shieh, Appl. Phys. Lett. **88**, 241115 (2006).

[17]L. Jochum and W. Meyer-llse, Appl. Opt. **34**, 4944 (1995).

[18]B. Lengeler, C. G. Schroer, M. Richwin, J. Tummler, M. Drakopoulos, A. Snigirev, and I. Snigireva, Appl. Phys. Lett. **74**, 3924 (1999).

[19]W. Chao, B. D. Harteneck, J. A. Liddle, E. H. Anderson, and D. T. Attwood, Nature **435**, 1210 (2005).

[20]G.-C. Yin, Y.-F. Song, M.-T. Tang, F.-R. Chen, K. S. Liang, F. W. Duewer, M. Feser, W. Yun, and H.-P. D. Shieh, Appl. Phys. Lett. **89**, 221122 (2006).

[21]T. Y. Chen, Y.-T. Chen, C.-L. Wang, I. M. Kempson, W.-K. Lee, Y. S. Chu, Y. Hwu, and G. Margaritondo, Opt. Express **19**, 19919 (2011).